Total and anthropogenic inorganic carbon fluxes in the Southern Ocean mixed layer from an eddying global ocean model

Simone Le Chevère[1,2], Carolina O. Dufour[2,3], Laurent Bopp[4], Marina Lévy[5]

[1]Alfred Wegener Institute, Helmholtz Centre for Polar and Marine Research, Bremerhaven, Germany
[2]Department of Atmospheric and Oceanic Sciences, McGill University, Montreal, Canada
[3]Univ. Brest, CNRS, IRD, Ifremer, Laboratoire d'Océanographie Physique et Spatiale (LOPS), IUEM, Brest, France
[4]Laboratoire de Météorologie Dynamique (IPSL), Paris, France
[5]Laboratoire d'Océanographie et du Climat: Expérimentations et Approches Numériques (IPSL), Paris, France

Key Points:

- We compute the total and anthropogenic inorganic carbon fluxes within the mixed layer of five regions of the Southern Ocean over 1995-2014.
- Advection dominates total carbon subduction across the mixed layer base but vertical diffusion contributes equally for anthropogenic carbon.
- Carbon subduction fluxes are intensified within the Antarctic Circumpolar Current and at major topographic features through advection.

Corresponding author: Simone Le Chevère, simone.lechevere@awi.de

Abstract

The Southern Ocean (SO) south of 35°S represents a small source of natural inorganic carbon for the atmosphere but a major sink of anthropogenic carbon. The magnitude of the total (natural plus anthropogenic) carbon sink strongly depends on the rate at which carbon is subducted below the mixed layer. We use a global ocean model at eddying resolution under preindustrial and historical conditions to provide a detailed view of total and anthropogenic dissolved inorganic carbon (DIC) pathways across and within the time-varying mixed layer of five physically consistent regions. Within each region, subduction fluxes at the mixed layer base are decomposed into advective and diffusive contributions to determine which process dominates. Total DIC is found to be obducted south of the Antarctic Circumpolar Current (ACC), transferred northward within the mixed layer and subducted north of the ACC. This results in a net obduction of 11.2 PgC/year, with advective processes dominating the total transfer (67%). Anthropogenic carbon is uptaken in all regions but anthropogenic DIC is mainly subducted north of the ACC, the carbon taken up in the south being advected northward within the mixed layer before being subducted. This subduction (1.05 PgC/year) is achieved mainly through advection and diffusion, which dominate respectively north and south of the Subantarctic Front. Advective subduction fluxes show strong zonal variations and are increased near major topographic features and boundary currents. Our results suggest that we need to untangle advective and diffusive pathways regionally in order to understand how carbon subduction will evolve.

1 Introduction

The Southern Ocean (SO) plays a dominant role in the global carbon cycle, as it is thought to be both a source of natural carbon dioxide (CO_2) to the atmosphere in winter and a major sink of anthropogenic carbon, accounting for up to 40% of the global ocean anthropogenic carbon sink (Gruber et al., 2019; Frölicher et al., 2015; DeVries, 2014; Sabine, 2004). This unique role of the SO in the global ocean carbon cycle is mainly achieved thanks to its unique circulation (Marshall & Speer, 2012; Lumpkin & Speer, 2007). Within and south of the Antarctic Circumpolar Current (ACC), the upwelling of the Circumpolar Deep waters (CDW) leads to significant carbon outgassing in the winter as these waters are rich in natural dissolved inorganic carbon (DIC) accumulated through remineralization (Gray et al., 2018; Talley, 2013; Mikaloff Fletcher et al., 2007). In contrast, CDW are poor in anthropogenic carbon due to the lack of exposure to the contemporary atmosphere (Graven et al., 2012; Orr et al., 2001). As a result, CDW absorb large amounts of anthropogenic carbon where they upwell (Toyama et al., 2017; Mikaloff Fletcher et al., 2006; Sarmiento et al., 1992). Part of the upwelled waters then head further south, where they contribute to the formation of denser waters within the Antarctic margins. The other part of the upwelled waters heads towards the North and transform into Antarctic Intermediate Water (AAIW) and Subantarctic Mode Waters (SAMW) to eventually subduct below Subtropical Waters (STW), bringing with them the carbon absorbed along the way (Gruber et al., 2019). On average, the Southern Ocean is estimated to be a carbon sink at all latitudes, the absorption of anthropogenic carbon dominating over the outgassing of natural carbon (Hauck et al., 2023; Gruber et al., 2019).

The efficiency of the SO carbon sink is ultimately limited by the carbon subduction rate, that is the rate at which carbon is transferred from the mixed layer to the ocean interior (Davila et al., 2022; Carroll et al., 2022; Bopp et al., 2015; Levy et al., 2013; Iudicone et al., 2011; Sarmiento et al., 1992). Once atmospheric CO_2 is taken up by the ocean, it is stored in the mixed layer in the form of DIC, where it partly remains subject to air-sea gas exchange. Only subduction below the mixed layer base can lead to sustainable sequestration on timescales that could reach decades to centuries, thus maintaining the size of the deep ocean carbon pool (Graven et al., 2012). The SO is known to be a region with a particularly large injection of both total (natural + anthropogenic) (Carroll et al., 2022; Levy et al., 2013) and anthropogenic carbon, representing more than 30% of the global injection of anthropogenic carbon to the ocean interior, thanks to the formation of intermediate waters (Davila et al., 2022; Bopp et al., 2015). Once subducted, carbon may be obducted back in the mixed layer, sometimes only a few years after subduction in regions where processes support the upward transfer of carbon-rich waters, such as frontal and boundary current regions (Toyama et al., 2017; Sallée et al., 2012).

DIC subduction rates depend on several physical processes whose contribution may oppose in some regions and over some time periods. These processes include vertical advection (mostly driven by Ekman pumping and suction), horizontal advection across the sloped mixed layer base (sometimes referred to as lateral induction), along-isopycnal diffusion induced by mesoscale eddies and smaller scale features, vertical diffusion due to turbulent mixing across the mixed layer base, and seasonal entrainment/detrainment due to fluctuations of the mixed layer with seasons (Bopp et al., 2015; Levy et al., 2013). These processes do not have the same magnitude and role for natural DIC, anthropogenic DIC, and as a consequence for total DIC. Using a 2° global ocean model, Levy et al. (2013) find that vertical advection dominates the transfer of natural DIC across the mixed layer base in the SO, leading to a net obduction, while obduction by vertical mixing is found to be one order of magnitude smaller. The authors also find that horizontal advection drives only a small part of natural DIC subduction and is partly countered by eddy mixing. In contrast, Dufour et al. (2013) find that vertical diffusion dominates over vertical advection for the obduction of natural DIC south of the Polar Front in a regional 0.5° ocean model. The physical transfer of anthropogenic DIC is found to be dominated by vertical mixing (mainly vertical diffusion) in ocean models (Toyama et al., 2017; Bopp et al., 2015). However, observation-based estimates of anthropogenic carbon subduction suggest that the role of vertical diffusion is negligible in regards to that of advection (Sallée et al., 2012). When looking at total DIC, Carroll et al. (2022) show that both advective and diffusive processes are important in subducting DIC across the base of the mixed layer. In a recent observational study using BGC-Argo float measurements, Sauvé et al. (2023) found an important role of mixing processes in obducting total DIC south of the ACC and within the sea ice covered region. Therefore, the relative roles of advection and vertical mixing in carbon subduction remain unclear.

While the deployment of hundreds of autonomous biogeochemical Argo floats (BGC-Argo) since the 2010s has improved the quantification of air-sea CO_2 fluxes in all seasons (Sauvé et al., 2023; Gray et al., 2018; Williams et al., 2017), carbon subduction rates and their driving processes remain difficult to quantify from observations. Estimates of mixing notably depend on the poorly constrained eddy diffusivity coefficient (Sauvé et al., 2023). Besides, the vastness of the Southern Ocean precludes any detailed spatial description of the carbon subduction fluxes, constraining observation-based estimates to be presented as quantities integrated over large regions. Carbon subduction does not, however, occur at the same rate across the SO. Regions of water mass formation within and north of the ACC are known to be particularly effective at subducting carbon (Davila et al., 2022; Mikaloff Fletcher et al., 2006). Within these regions, observations suggest localized sites of subduction and reventilation of anthropogenic carbon located next to each other, in particular where the mixed layer is sloped with respect to the mean flow (Sallée et al., 2012). This heterogeneous spatial distribution in the subduction rates of natural and anthropogenic carbon driven by lateral advective fluxes also clearly appear in numerical models (Bopp et al., 2015; Levy et al., 2013). In contrast, diffusive fluxes of carbon generally show a more homogeneous distribution across the Southern Ocean with the exception of western boundary currents where enhanced fluxes are found (Carroll et al., 2022; Bopp et al., 2015; Levy et al., 2013).

In front of the lack of observations to get accurate estimates of carbon subduction fluxes, numerical models have been used to obtain a quantification of these fluxes. The models used, however, have been generally too coarse to explicitly resolve mesoscale eddies (Levy et al., 2013; Bopp et al., 2015). Previous studies have shown that eddy-permitting models give better estimates of oceanic storage of anthropogenic DIC than their lower resolution counterparts (Terhaar et al., 2019; Lachkar et al., 2007). In models, parameterization of the mesoscale eddy transport has a significant impact on the subduction of carbon, and hence on the quantity of carbon taken up from the atmosphere (Doney et al., 2004). In addition to impacting the magnitude and patterns of subduction fluxes, an increased resolution is likely to impact the respective roles of physical processes in transferring carbon to the ocean interior. Particularly in the SO, where the ACC spawns a vigorous eddy field, resolving mesoscale eddies or parameterizing their effect in ocean models leads to large differences in the mixed layer depth, the meridional overturning circulation and affects the pathways and time scales of deep water upwelling (Drake et al., 2018; Tamsitt et al., 2017; Dufour et al., 2012; Marshall & Speer, 2012; Hallberg & Gnanadesikan, 2006). Besides, the restratification of the water column induced by eddy-driven transport is expected to play a role in anthropogenic carbon subduction (Sallée et al., 2012), and the advection of tracers by the mean circulation is strongly compensated by eddy-driven advection, thus reducing the transport of natural DIC towards the surface (Dufour et al., 2013). Indeed, advective subduction fluxes are found to be countered by the eddy-induced subduction in models (Levy et al., 2013; Bopp et al., 2015) and observational estimates (Sallée et al., 2012). Eddies can also enhance the transfer of tracers from and to the ocean interior in localized regions with high eddy kinetic energy (Brady et al., 2021; Balwada et al., 2018). Therefore, it appears that an investigation of the magnitude and patterns of carbon subduction requires to take into account mesoscale eddies.

In this study, we use a global eddying ocean-sea ice model to perform a detailed budget of total and anthropogenic carbon within the mixed layer and investigate the processes that drive the subduction of carbon across the base of the mixed layer in five physically consistent regions of the SO. Two simulations are run, one under preindustrial conditions and one under historical conditions to obtain the anthropogenic component of carbon, and an online diagnostic of subduction fluxes across the time-varying mixed layer is performed to allow an exact decomposition of the physical drivers of the inorganic carbon fluxes.

2 Methods

2.1 Model and simulations

2.1.1 The eORCA025-PISCES global configuration

We use the NEMO (Nucleus for European Modelling of the Ocean) model platform, which comprises the ocean general circulation model OPA ("Océan Parallélisé") developed by Madec et al. (1998). OPA is coupled with the thermodynamical and dynamical Louvain-la-Neuve sea Ice Model (LIM3) which features five ice categories, each divided into one layer of snow and five layers of ice (Vancoppenolle et al., 2009). The ocean model includes the biogeochemical component Pelagic Interaction Scheme for Carbon and Ecosystem Studies (PISCES) (Aumont et al., 2015) which holds 24 prognostic tracers. PISCES includes two phytoplankton functionnal types (diatoms and nanophytoplankton), two zooplankton size-classes (micro- and mesozooplankton), and five nutrients which are phosphate (PO_4), ammonium (NH_4), nitrate (NO_3), silicium (Si) and iron (Fe). In addition, PISCES includes four prognostic carbon variables: DIC, dissolved organic carbon (DOC), particulate organic carbon (POC) and particulate inorganic carbon (PIC), as well as alkanity. The DIC concentration is partitionned into three species ($\mathrm{DIC}=\mathrm{HCO}^-_{3(aq)}+\mathrm{CO}^{2-}_{3(aq)}+\mathrm{CO}_{2(aq)}$) following the Ocean Carbon-Cycle Model Intercomparison Project protocols (Orr et al., 2017). CO_2 sea-air fluxes are computed following Wanninkhof (1992):

$$F_{CO_2} = (1 - f_{ice}) \times K(pCO_2^{ocean} - pCO_2^{atm}) \quad (1)$$

with K the gas transfer velocity depending mainly on the temperature and the wind speed, the partial pressure of CO_2 in the ocean (pCO_2^{ocean}) and in the atmosphere (pCO_2^{atm}), and f_{ice} the sea ice total fraction.

The eORCA025 global configuration is used to run the model (Madec & the NEMO Team, 2016). This configuration has a tripolar grid with a global orthogonal curvilinear ocean mesh applied to a Mercator projection. The nominal horizontal resolution is 0.25° resulting in grid sizes of around 17 km at 50°S and 5.6 km (zonal direction) and 3.2 km (meridional direction) at the highest latitudes (Madec & the NEMO Team, 2016). Antarctic under-ice shelf seas are represented to account for the contribution of the ice-shelf–ocean interactions to the SO freshwater cycle (Mathiot et al., 2017). In the vertical, the water column is split in 75 levels with grid thickness increasing from 1 m at the surface to around 200 m at the bottom. The 0.25° resolution only allows for the partial resolution of mesoscale eddies in the Southern Ocean (Hallberg, 2013). Hence, the parameterizations of Gent and McWilliams (1990) and Redi (1982) are used with small coefficients of 300 $m^2\ s^{-1}$ and 100 $m^2\ s^{-1}$, respectively, to obtain physical and biogeochemical fields that remain close to observations while maintaining an explicit representation of oceanic mesoscale features. In coarser resolution configurations, those coefficients are typically set to much larger values: for example, both coefficients are set to 2000 $m^2\ s^{-1}$ in ORCA_R2, the 2° resolution counterpart of ORCA025 (Bopp et al., 2015).

2.1.2 Preindustrial and historical simulations

Two simulations are run with the eORCA025-PISCES configuration: one with preindustrial atmospheric CO_2 conditions (PIND) and one with historical CO_2 conditions (HIST), following the Global Carbon Budget (GCB) (Hauck et al., 2020). In PIND, an atmospheric CO_2 concentration of 278 ppm, corresponding to the year 1850, is kept constant throughout the simulation. PIND is initialized from GLODAPv2 preindustrial DIC field (Olsen et al., 2016). In HIST, the atmospheric CO_2 concentration follows the GCB time series (Friedlingstein et al., 2020). HIST is initialized in 1958 with GLODAPv2 total DIC concentrations computed by adding to the preindustrial DIC field the anthropogenic DIC field from year 1958 of an ORCA05 simulation from Terhaar et al. (2019). Both simulations are run from 1958 to 2014 using the atmospheric fields from the Drakkar forcing set 5 version 2 (DFS5) (Dussin et al., 2016), which has been designed explicitly for running ocean-only simulations and exists until 2014. Subtracting PIND from HIST enables to obtain the anthropogenic component of carbon in the ocean. As the simulated ocean circulation is the same in PIND and HIST, this approach allows to investigate the passive penetration of anthropogenic carbon into the ocean.

2.2 Observation products

To evaluate the modelled sea-air CO_2 fluxes, we use the observation-based product presented in Bushinsky et al. (2019). This product combines the pCO_2 climatology of the Surface Ocean CO_2 Atlas (SOCAT) (Landschützer et al., 2020) from 1982 to 2017 and the SOCCOM dataset from Gray et al. (2018) with Argo-float data collected between 2014 and 2017, and uses a neural network method to reconstruct pCO_2 (Landschützer et al., 2013) during the period 2015 - 2017. We also use the CO_2 flux climatology from the Global Carbon Budget (Hauck et al., 2020).

The modelled carbon storage is assessed against that computed from GLODAPv2 (Lauvset et al., 2016). DIC content is gravimetric in GLODAPv2 while it is volumetric in our model. Therefore, we convert the mol/kg into mol/m^3 by multiplying by the constant in situ density of 1028 kg/m^3 used in NEMO (see Planchat et al. (2023)).

To evaluate the salinity and the potential temperature in the model (and hence the potential density), we use the CORA5.2 dataset of Szekely et al. (2019) which is based on Argo floats measurements combined with CTD casts from several programs and the World Ocean Database 2013 (WOA) between the years 1995-2014 (Locarnini et al., 2013; Zweng et al., 2013). Finally, mixed layer observations are provided by a climatology that includes Argo floats profiles taken from 2001 to 2015 (Hosoda et al., 2010).

2.3 Analyses

2.3.1 Southern Ocean regions

In order to compare the modelled sea-air CO_2 fluxes to observational estimates, we use the five Southern Ocean regions defined in Gray et al. (2018) for all of our analyses. Each region corresponds to a different dynamical and biogeochemical province of the Southern Ocean south of 35°S and each boundary is averaged over the 20-year period of 1995-2014. The boundaries of the regions are defined using the dynamical and biogeochemical characteristics of our model to ensure consistency with the model solution. The five regions are defined as follows (see also Fig. 1):

- *The Sea Ice Zone (SIZ)* is defined as the region where the September sea ice concentration is greater than 15% and is bounded at the north by the Sea Ice Front (SIF).
- *The Antarctic Southern Zone (ASZ)* is located between the SIF and the Polar Front (PF). The PF location is defined using a sea surface height (SSH) contour identified at a local maximum of SSH meridional gradient. This local maximum is searched for within a [-0.5°;+2°] band around the northernmost location of the 2°C isotherm between 50 m and 300 m. This latter location is used to track the equatorward penetration of the Antarctic Winter Waters (Park et al., 1998). The SSH contour selected to define the location of the PF is computed as the average of 10 SSH contours each defined at different longitudinal sections across the SO following Dufour et al. (2015).
- *The Polar Frontal Zone (PFZ)* is located between the PF and the Subantartic Front (SAF). The SAF location is defined using a SSH contour identified at a local maximum of SSH meridional gradient. This local maximum is searched for within a latitudinal band varying from 1° to 10° (depending on the longitudinal section) south of the winter mixed layer depth (MLD) maximum found north of the ACC. This maximum identifies the region of formation of Subantarctic Mode Waters (Li et al., 2021; Orsi et al., 1995). The SSH contour of the SAF is computed as the average of 8 SSH contours each defined at different longitudinal sections across the SO, similarly to the PF (but excluding two locations where the SAF was not clearly distinct).
- *The Subantarctic Zone (SAZ)* is located north of the SAF and south of the Subtropical Front (STF). The STF corresponds to the location of the 11°C isotherm of conservative temperature at 100 m following Orsi et al. (1995).
- *The Subtropical Zone (STZ)* is defined north of the STF and south of 35°S, the northernmost extent of our domain.

When comparing the areas of our regions to that of Gray et al. (2018), we find differences of the order of 5% to 18% (Table 1). These differences are due to discrepancies in coastal resolution which partially explains the larger areas of the SIZ and STZ that we obtain. The rest of the differences are explained by slightly different definitions used for the PF and SAF and to the biases in the model solutions.

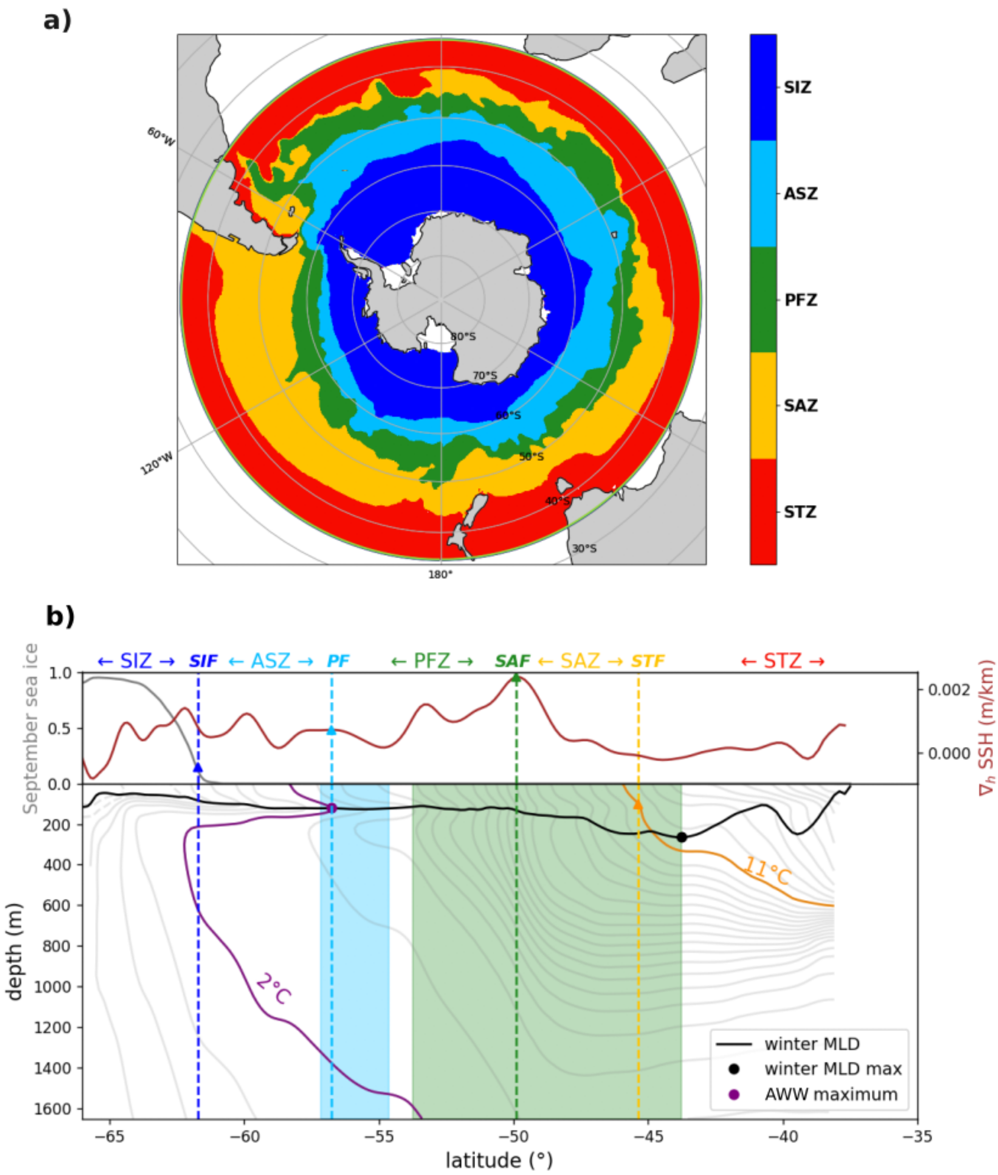

Figure 1. a) The five regions of the Southern Ocean used in the study. From South to North: Sea Ice Zone (SIZ), Antarctic Southern Zone (ASZ), Polar Frontal Zone (PFZ), Subantarctic Zone (SAZ), and Subtropical Zone (STZ). b) Example of the boundary detection procedure for 140°E, one of the meridional sections used to define the PF and SAF. The SIF, PF, SAF and STF are represented in dotted lines. In the top panel, the September sea ice fraction is represented in grey, with the triangle at 0.15 marking where we define the SIF. The potential temperature is contoured in the background of the bottom panel with the 2°C isotherm highlighted in purple along with the northernmost extent (purple dot) corresponding to the Antarctic Winter Waters (AWW). The [-0.5°,2°] band (blue shading) is the region where a local maximum in the SSH meridional gradient (brown curve in the top panel) is searched for. The location of this maximum defines the location of the PF (light blue triangle). Note that in this example the purple dot and light blue triangles align but that is not necessarily the case for every section investigated. The winter MLD (black curve; bottom panel) shows a maximum north of the ACC. A 10° latitudinal band south of this maximum (green shading) is defined to search for the local maximum of the SSH meridional gradient corresponding to the location of the SAF (green triangle; top panel). Finally, the latitude where the 11°C isotherm (orange curve) crosses the 100 m isobath (orange triangle) defines the location of the STF.

Table 1. Areas of the five regions of the SO (in 10^7 km^2) in the eORCA025 model and in observations (Gray et al., 2018), and relative differences between the model and observations. Definitions are detailed in Section 2.3.1 and the regions are represented in Fig. 1.

	SIZ	ASZ	PFZ	SAZ	STZ	Total
eORCA025	2.03	1.47	1.25	2.04	2.48	9.27
Gray et al. (2018)	1.72	1.28	1.43	1.94	2.26	8.64
Rel. error (%)	18	15	-13	5	10	7

2.3.2 Carbon budgets in the mixed layer

Carbon budgets in the mixed layer are computed offline for each of our five regions as follows:

$$\frac{\partial C}{\partial t} = -F_{C,sea-air} + F_{C,sub} - \nabla_h F_{C,bound} + Residual \tag{2}$$

with $\partial C/\partial t$ the tendency of tracer C (here the DIC) in the mixed layer, $F_{C,sea-air}$ the CO_2 sea-air fluxes, $F_{C,sub}$ the upward subduction of DIC at the mixed layer base, and $\nabla_h F_{C,bound}$ the horizontal divergence of DIC fluxes across the region boundaries. Horizontal fluxes of carbon are computed at each boundary (at the fronts or at 35°S) using monthly averaged horizontal velocities and tracer concentration for total DIC. The *Residual* term for total DIC includes biological processes, river runoff and horizontal diffusion that are not accounted for here due to the lack of the necessary model output. It also includes errors resulting from the offline computation of horizontal fluxes. For the budget of anthropogenic DIC, each term is computed from the difference between the budget terms of the total and natural DIC (using Eq. 2) except for horizontal divergence which is computed as a residual term. We do so as, in the case of anthropogenic carbon, the residual term does not include biological processes nor river runoff given that they remain the same between the HIST and PIND simulations. In any case, the horizontal diffusion is considered negligible. All results are presented averaged over the period 1995-2014 (the last twenty years of our simulations).

2.3.3 Computation of subduction fluxes of carbon

The subduction of DIC is computed online at every time step of the model across the time-varying mixed layer base from the sum of several fluxes that we combine following Karleskind et al. (2011); Levy et al. (2013) and Bopp et al. (2015):

$$F_{C,sub} = \int_t (\underbrace{-C_h(w_h + \boldsymbol{u}_h.\boldsymbol{\nabla} h) + F_{C,GM}}_{\text{total advection}} + \underbrace{k_z^h \partial_z C_h}_{\text{vertical diffusion}} \underbrace{-C_h \partial_t h}_{\text{seasonal entrainment}} + \underbrace{F_{C,Redi}}_{\substack{\text{Parameterized}\\ \text{isopycnal diffusion}}})dt \tag{3}$$

The *total advection* term is the total (vertical and horizontal) advection of tracer C (here the DIC) through the base of the mixed layer, where C_h is the concentration of DIC, w_h and $\mathbf{u}_h$ are respectively the vertical and horizontal velocity at the base of the mixed layer (subscript h), and $F_{C,GM}$ the subduction by the parameterized eddy driven transport (Gent et al., 1995). $F_{C,GM}$ represents only around 5% of the total advection term given that the coefficient used is relatively small (see Section 2.1). For this reason, we combine the parameterized and resolved advection term in our analysis. The *vertical diffusion* term corresponds to the vertical diffusion of tracer C across the mixed layer base, with k_z^h the vertical diffusion coefficient and $\partial_z C_h$ the vertical gradient of C across the base of the mixed layer. Vertical diffusion coefficients k_z^h are derived from the Turbulent Kinetic Energy (TKE) closure scheme of Blanke and Delecluse (1993) with improvements from Madec (2008) and vary around 1.2 10^{-5} m^2 s^{-1}. The *seasonal entrainment* term is the entrainment/detrainment of C due to the temporal variations of the MLD h. Finally, the *parameterized isopycnal diffusion* term, $F_{C,Redi}$, corresponds to the along-isopycnal diffusion of C at the mixed layer base (Redi, 1982).

2.4 Evaluation of the simulations

2.4.1 Mixed layer depth and stratification

In the model, the spatial distribution of the MLD is overall similar to that of the observations (Fig. 2a-e). In particular, deep MLD patterns in the East Pacific and Indian sectors are well represented, with a moderate downstream (eastward) shift of the deepest MLD compared to observations (Fig. 2c-d). The deep MLD found in the model south of the South African coast in the STZ, however, does not appear in observations. We find that in both summer (January) and winter (August), the modelled MLD is on average shallower than the observed MLD by ∼10 m and ∼20 m, respectively, between 35°S and 70°S. The shallow summer bias likely comes from a lack of wind energy input in our model or from the vertical mixing parameterization scheme that does not account for some wind effects (e.g. swells, near-inertial oscillations) (Rodgers et al., 2014). Deep bias is generally found in non-eddying and eddy-permitting models in winter due to the lack of restratification by mesoscale eddies. Refining the horizontal resolution and/or adding a mesoscale eddy transport parameterization both act in reducing this bias (Adcroft et al., 2019). Running our model with both parameterization and eddy-permitting resolution might be the reason for the absence of this bias.

The model generally reproduces a stratification similar to that observed (Fig. 2.f-g). We note, however, a high bias in salinity in the upper and subsurface ocean of the model that impacts the representation of AAIW (see also Fig. S1.d). There is also a low bias in density at depth south of 60°S which is typical of z coordinate models which are known to have a poor representation of the processes leading to the overflow and sinking of dense shelf waters along the Antarctic continental slope (Adcroft et al., 2019).

2.4.2 Sea-air CO_2 fluxes

Over 2009-2014, -1.13±0.05 PgC/year of CO_2 is absorbed by the ocean south of 35°S in the model (Fig. 3). CO_2 is taken up in all regions of the SO, including south of the ACC, in accordance with observations from SOCAT, while SOCAT+SOCCOM combined data give an outgassing in the ASZ. When averaged over the SO, the total uptake is found to be very similar to the SOCAT estimate, but it results from a compensation between a higher uptake south of and within the ACC (SIZ, ASZ, PFZ) and a lower uptake north of the ACC (SAZ, STZ). When compared to the SOCAT+SOCCOM dataset, the model shows a higher uptake in all regions but the STZ. The SOCCOM dataset shows an ougassing in the SIZ and ASZ, in contrast to the SOCAT dataset and most biogeochemical ocean models: this disagreement was hypothesized to arise from the year-round sampling of BGC-Argo floats in this region or to biases in the float pH measurements (Gray et al., 2018; Bushinsky et al., 2019; Maurer et al., 2021). A caveat on this analysis is that we use the time period 2009-2014, while the SOCCOM+SOCAT data and the SOCAT data span over the period 2015-2017 Bushinsky et al. (2019)). Given the decadal variability in CO_2 (Landschützer et al., 2016), comparing estimates spanning different time periods might be one of the main source of disagreement between these different products. Finally, while the modelled sea-air fluxes evolve within the range of estimates provided by the Global Carbon Budget (GCB) over 1995-2014 below 35°S, they show

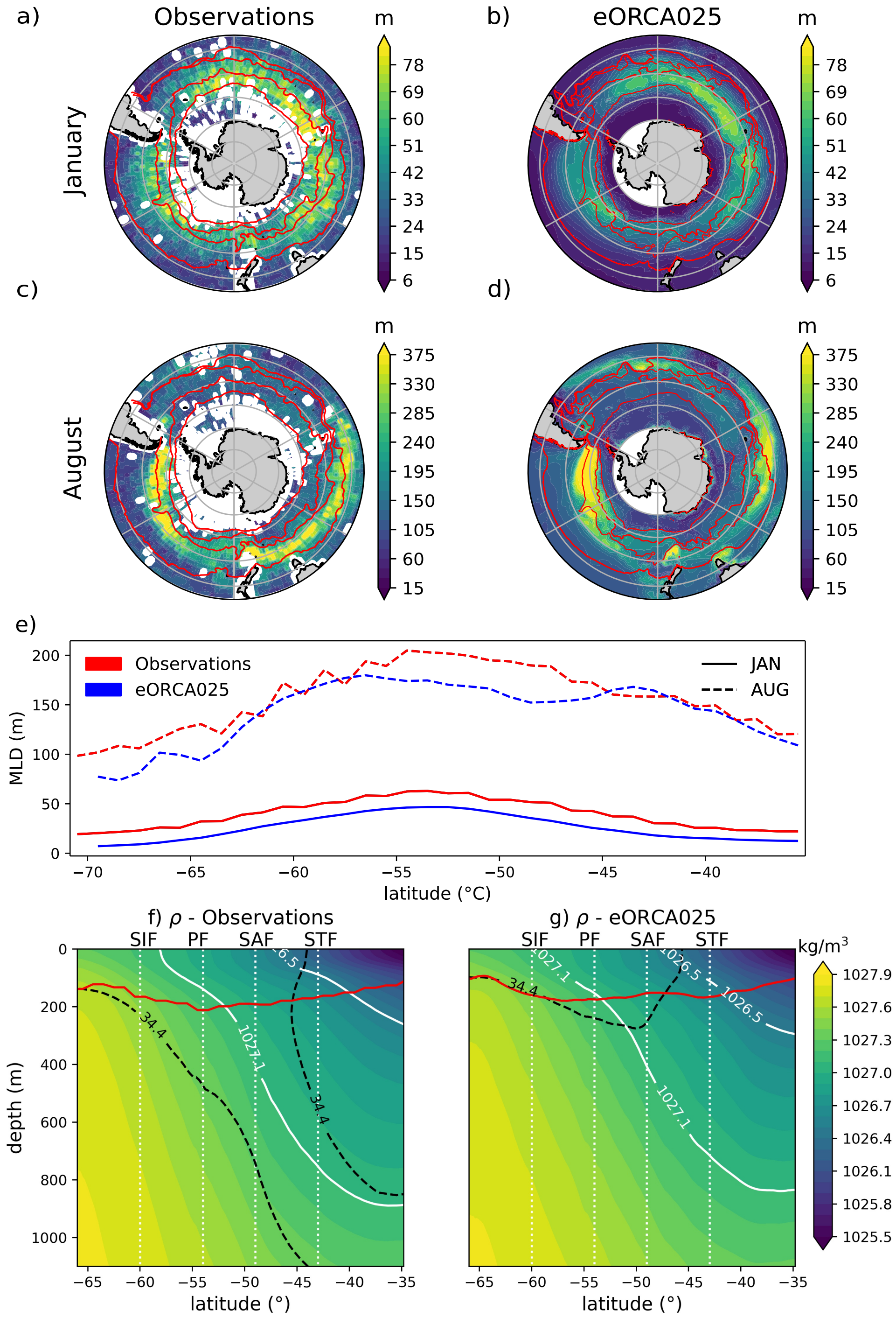

Figure 2. MLD for (a,b) January (month of the shallowest mixed layer) and (c,d) August (month of the deepest mixed layer) averaged over the period 1995-2014 (our model) and 2001-2015 (observations). This time period is the best overlap between the observational dataset and simulation time periods. Observations (a and c) are from Hosoda et al. (2010) and are based on Argo floats measurements using the density criterion of $\Delta\sigma = 0.03$ kg m^{-3} following de Boyer Montégut (2004). The boundary of the five regions are represented with red contours using the observation-based boundaries from Gray et al. (2018) in (a,c) and the method described in Section 2.3.1 and applied to the model output in (b,d). (e) shows the zonal average of MLD in our model and the observations for both January and August. Potential density referenced to the surface (background and white contours) in (f) our model and (g) derived from in situ temperature and salinity observations from the CORA5.2 dataset (Szekely et al., 2019) using the eos80-seawater python package, averaged over 1995-2014. Black dotted lines correspond to the salinity (PSU) and highlight the location of the AAIW. Red lines correspond to the MLD in (f) model and (g) observations from Hosoda et al. (2010)

.

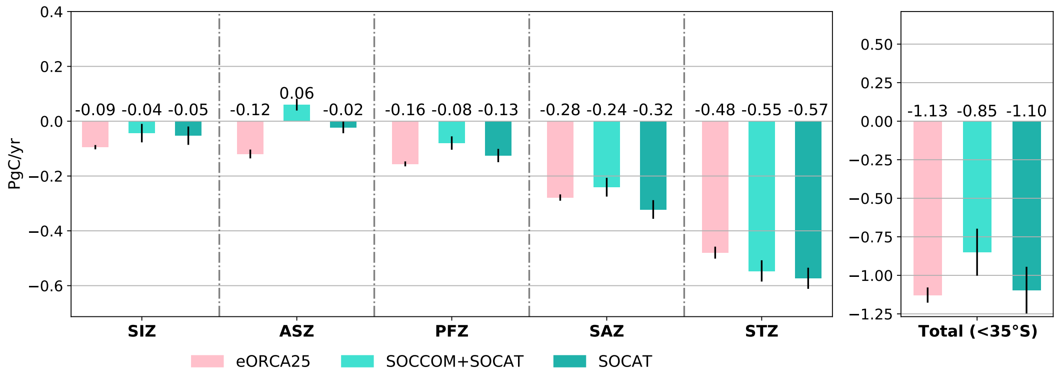

Figure 3. Sea-to-air CO_2 fluxes integrated over (left) each of the five regions defined in Section 2.3.1 and (right) the Southern Ocean (south of 35°S) in the HIST simulation (pink) and two observation products (green): the SOCAT dataset (Bakker et al., 2016) and the combination of SOCCOM and SOCAT datasets by Bushinsky et al. (2019). Positive fluxes correspond to outgassing. Model fluxes are integrated between 2009 and 2014, while observations reflect measurements from 2015 to 2017 Bushinsky et al. (2019). Error bars correspond to interannual variability in the model, and combine the interannual variability and a method uncertainty of ±0.15 Pg C in Bushinsky et al. (2019). Note that the vertical scale is different between the five regions (left) and the Southern Ocean (right).

an increase at a slightly faster rate (3.5 10^{-10} mol/m^2/s/year when linearly fitted between 1965 and 2014) than the average of GCB models (3.1 10^{-10} mol/m^2/s/year), which indicates a stronger sink (Fig. S2).

2.4.3 DIC fields

Our model generally shows a smaller total DIC concentration within the DIC-rich CDW compared to observations (Fig. 4a-b), with a maximum difference at around 250 m depth. This difference might result from a higher stratification (Fig. 2.f) and a weaker upwelling of dense and DIC-rich deep waters in the model. In contrast, the DIC is found to be higher in the model below 600 m in the SAZ and STZ within the AAIW. These differences may arise from weaker ventilation of these waters in our model (Fig.2 f,g), a bias also found in CMIP6 models (Hong et al., 2021). Subtropical Waters (STW) have a lower DIC concentration (below 2100 mmol.m^{-3}), and show a large negative bias in the model at around 150 m, due to a larger penetration of the DIC-poor STW at depth at 35°S compared to observations. Finally, surface waters show higher DIC concentrations in all regions of the model compared to observations, possibly due to the higher stratification found in the model (Fig. 2e) and an anomalously high uptake of CO_2 (Fig. 3).

For the anthropogenic DIC, differences with observations are more uniform with the model generally showing a negative bias, except around 200 m depth in the STZ (Fig. 4c-d). The negative bias is strongest within the CDW and the AAIW, with a maximum between 400 m and 900 m in the PFZ. Similarly to the total DIC, this low bias might arise from a weak penetration of AAIW and SAMW into the interior, as it was inferred in other studies (Bourgeois et al., 2022). This reduced penetration is found in most global biogeochemical ocean models (Hauck et al., 2023) and occurs despite a relatively high surface salinity (Fig. S1), that was shown to lead to the formation of denser AAIW and

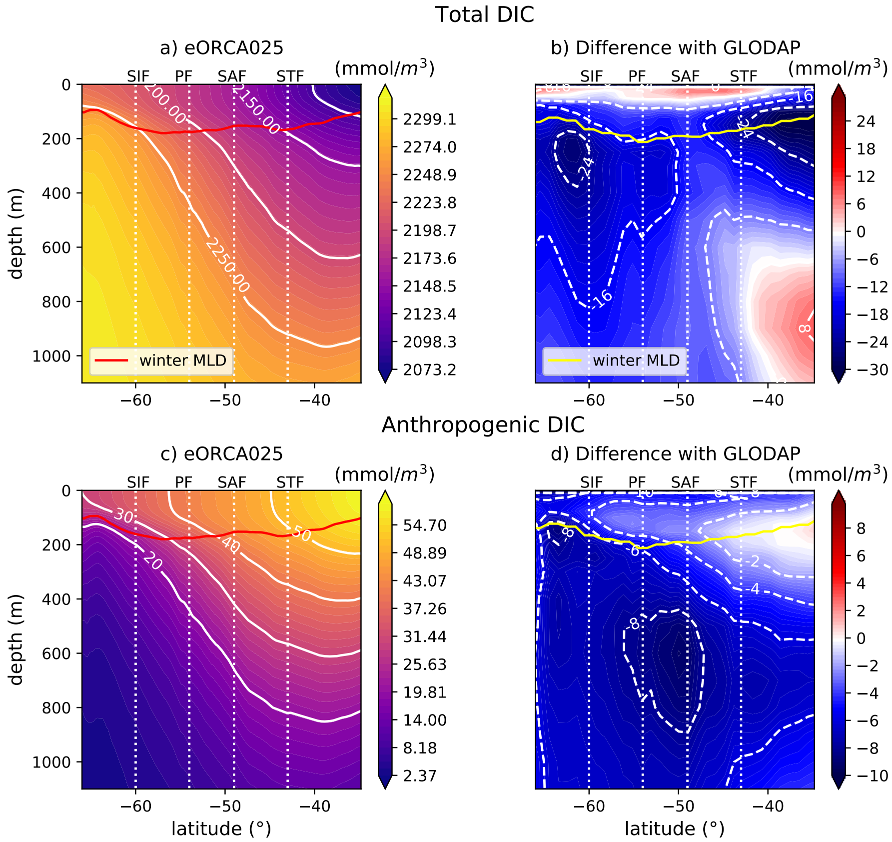

Figure 4. Zonally averaged cross-section for (a) total and (c) anthropogenic DIC in the model, and (b,d) corresponding difference (model - observations) with the observation-based GLODAPv2 (Lauvset et al., 2016). The winter MLD is indicated in red for the model (a,c) and in yellow for the observations (b,d). MLD estimates are taken from Hosoda et al. (2010). Locations of the averaged latitudes of the fronts in the model are indicated by white-dotted lines, while white contours correspond to the DIC concentrations.

hence to more anthropogenic carbon uptake in this region (Terhaar et al., 2021). The high bias in the STZ in the upper 200 m, on the other hand, mirrors the low bias found in this region in the total DIC and likely originates from the large penetration of relatively young STW into the Southern Ocean through boundary currents. Part of the low bias found in the modeled anthropogenic DIC fields might also come from the fact that the field is initialized at 0 mmol/m^{-3} in 1850 while anthropogenic carbon content has been shown to amount to 11 PgC globally at that time (Terhaar et al., 2024).

3 Results

3.1 Fluxes of total Dissolved Inorganic Carbon within the mixed layer

3.1.1 Budget within the mixed layer

In the SO mixed layer, the budget of total DIC (DIC$_{tot}$) primarily results from the export/import of DIC$_{tot}$ across the mixed layer base and a redistribution of DIC$_{tot}$ between the regions. Over the SO, DIC$_{tot}$ is brought at a rate of 11.2 PgC/year within the

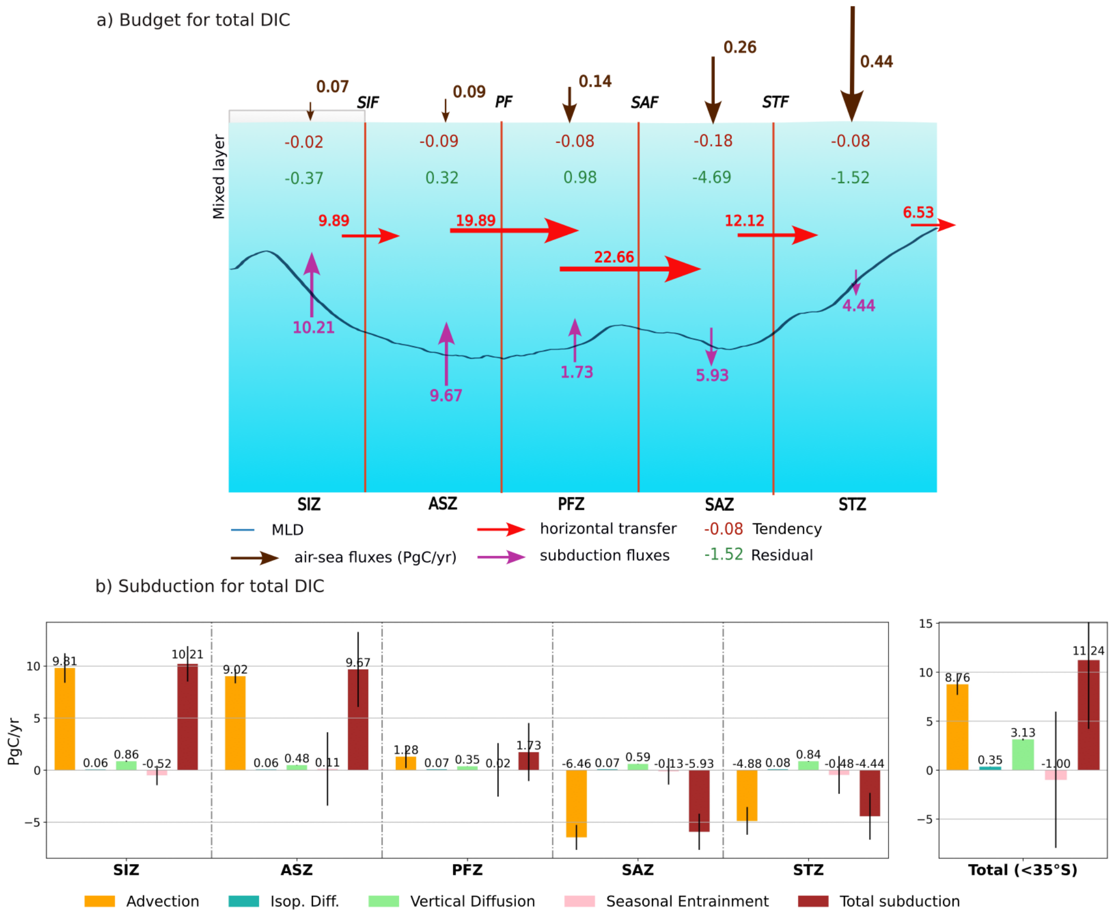

Figure 5. (a) Budgets of total DIC in the mixed layer averaged over 1995-2014 for each of the five regions of the SO (see definition in Section 2.3.1). The budget terms are computed following Eq. (2) and expressed in PgC/year. The size of arrows used for horizontal and mixed layer fluxes is 1/40 compared to the scale used for air-sea fluxes. Positive values in the mixed layer indicate a gain of DIC. (b) Decomposition of subduction fluxes across the base of the mixed layer for each region into the different processes following Eq. (3). Positive fluxes correspond to obduction of DIC within the mixed layer. Error bars correspond to the interannual variability over 1995-2014.

mixed layer as a result of a large obduction of 21.6 PgC/year south of the SAF compensated by a comparatively weaker subduction of 10.4 PgC/year north of the SAF. Once obducted in the mixed layer of the SIZ and of the ASZ, and to a lesser extent of the PFZ, DIC_{tot} is transported northward across the fronts of the ACC (Fig. 5a). These fluxes are consistent with the physical circulation and large-scale DIC gradients in the SO (Gruber et al., 2019; DeVries et al., 2017). Almost half of the DIC_{tot} transported north of the SAF within the mixed layer is subducted to the ocean interior within the SO. The other half is transported north of 35°S (6.53 PgC/year), that is out of the SO, or is removed most likely by biological processes within the SAZ and STZ (6.21 PgC/year). Our results thus show a consistent northward transport of DIC across all fronts of the ACC implying that most of the DIC found in the STZ mixed layer is of SO origin. This result contrasts with that of Iudicone et al. (2011) who find that natural DIC is imported to the SO from low latitudes within the mixed layer (their Fig. 3 and Fig. 6). Whether this discrepancy arises from the Lagrangian method used in Iudicone et al. (2011) or from the model solution is unclear.

Air-sea fluxes are generally very small compared to the DIC_{tot} transport terms within and at the base of the mixed layer, but provide a comparatively bigger contribution in the northernmost regions due to enhanced fluxes in western boundary currents and in the subtropical Atlantic Ocean (Fig. S3). Overall, even though large amounts of DIC_{tot} are brought to the mixed layer by upwelled Pacific, Indian and North Atlantic Deep Waters, it is not transferred to the atmosphere and is instead transported northward and then largely subducted north of the ACC, in agreement with previous results (DeVries et al., 2017). The residual term of the budget is relatively small compared to the fluxes across the regions and the base of the mixed layer but comparable to the air-sea fluxes. This term comprises the sources and sinks of DIC_{tot} due to biological processes, the DIC input from rivers as well as errors in the calculation of the budget terms (see Section 2.3.2). The largest residual terms are found in the SAZ and the STZ (Fig. 5a), which is due to a higher biological activity and more DIC input from rivers in these regions (not shown).

Over 1995-2014, no significant net accumulation nor loss of DIC_{tot} occurs in the mixed layer of the SO (Fig. S4.a), and no significant trend occurs either in any of the DIC fluxes within or across the mixed layer and at the surface in any region of the SO. This lack of long-term trend may result from the relatively short time period investigated and may be explained by a comparatively large decadal variability driven by oceanic and atmospheric forcings (Landschützer et al., 2016). The muted interannual variability of the DIC_{tot} tendency is not in line with the results of Carroll et al. (2022), who find this term to be significantly increasing in their SO subtropical biome. However, they also show that the DIC tendency is small in the Southern Ocean compared to other regions (their figure 6).

3.1.2 Physical drivers of the subduction

In the model, the transport of DIC_{tot} across the base of the mixed layer is found to be dominated by advection which represents the major part (>80%) of obductive fluxes south of the SAF, and of subductive fluxes north of the SAF (Fig 5b). Therefore, advection appears to be the dominant driver of subduction in all regions, but due to compensation between obductive fluxes in the south and subductive fluxes in the north, it only represents 67% of the transfer of DIC across the base of the mixed layer south of 35°S (Fig. 5b). The other important contributor SO-wide is vertical diffusion which accounts for 23% of the total physical transfer of DIC_{tot} across the mixed layer base of the SO. Despite being about an order of magnitude smaller than the advective term within regions (Fig 5b), the vertical diffusive term consistently brings carbon into the mixed layer of all regions (as DIC_{tot} increases with depth), providing an important pathway for carbon to the mixed layer at the scale of the SO. The contribution of this term is biggest in the SIZ and the STZ where vertical mixing can be enhanced by strong gradients across the base of the mixed layer (SIZ; see Fig. 4a,b) or intensified turbulent mixing in western boundary currents (STZ). The remaining fluxes of DIC_{tot} across the mixed layer base, seasonal entrainment and isopycnal diffusion, account for a very small fraction of the transfer within all regions, amounting to only 10% of the transfer over the SO. Of the two terms, isopycnal diffusion is the smallest and is mostly driven by its vertical component (not shown) which depends on the vertical gradient of DIC across the base of the mixed layer and on the mixing coefficient computed through the Redi isopycnal mixing parameterization. The seasonal entrainment term, while being generally several times bigger than the isopycnal diffusion term, has a relatively small contribution over the period due to a large interannual variability showing positive and negative contributions compensating over the years (Fig. 5b).

At the seasonal scale, the entrainment term also shows a large variability which dominates that of the total subduction of DIC_{tot} across the mixed layer base in all regions of the SO (Fig. S6). A peak of subduction occurs at the beginning of spring concurrent with a shoaling of the mixed layer and a strong obduction occurs in fall - winter as the mixed layer deepens. The seasonal cycle in the advective term is muted except in the SAZ and STZ where the subduction weakens (SAZ) or even reverses to an obduction (STZ) in the winter. Diffusive fluxes also generally show a weak seasonal cycle except in the southernmost and northernmost regions where the seasonally is opposite. In the SIZ, vertical diffusion is the strongest in the summer when the mixed layer is the shallowest.

3.2 Fluxes of anthropogenic Dissolved Inorganic Carbon within the mixed layer

3.2.1 Budget within the mixed layer

In the SO mixed layer, the budget of anthropogenic DIC (DIC_{anth}) results from the air-sea fluxes of anthropogenic CO_2, the export/import of DIC_{anth} across the mixed layer base and a redistribution of DIC_{anth} between the regions. Air-sea fluxes are the primary source of DIC_{anth} in the mixed layer with an uptake at the surface that ranges from 0.13 PgC/year to 0.18 PgC/year across the five regions (Fig. 6a). This small range between regions arises in part from compensation between intensity of fluxes and sizes of regions. In particular, the ASZ is the smallest zone and shows the largest fluxes of all five regions while the STZ is $\sim$70% larger with only about half the magnitude in air-sea fluxes (see table S1). The primary sink of DIC_{anth} in the SO mixed layer is the subduction of DIC_{anth} which amounts to 1.05 PgC/year (Fig. 6b). 71% of the subduction of DIC_{ant} in the SO occurs in the SAZ and the STZ, explaining the deep penetration of the anthropogenic signal seen in these regions (Fig. 4c). In contrast, the SIZ, the ASZ and to a lesser extent the PFZ show subduction rates around four times smaller than that of the northernmost regions. The DIC_{anth} uptaken at the surface of the SO represents 81% of the subducted DIC_{anth}, the remaining 19% being brought from the subtropical regions north of 35°S (14%) or from carbon already stored in the mixed layer (5%). More specifically, our analyses show that the Ekman transport brings DIC_{anth} northward in the SIZ, ASZ and PFZ, while a southward transport associated with western boundary currents brings DIC_{anth} from the subtropical regions north of 35°S into the STZ (Fig. 4). These horizontal and subduction fluxes lead to small accumulations of DIC_{anth} within the mixed layer of the SAZ and the STZ, where most of the subduction occurs, while keeping the southernmost regions depleted and hence more prone to take up anthropogenic carbon.

Over 1995-2014, air-sea fluxes of anthropogenic CO_2 show a significant positive trend ($r^2 > 0.85$ and p-value < 0.05) in all regions, as expected from the increase in atmospheric pCO_2 (Fig. S5.a), the highest increase happening in the STZ and the smallest in the ASZ. Yet, no net accumulation of DIC_{anth} occurs in the mixed layer of the SO meaning that the newly absorbed anthropogenic carbon is exported out of the SO within the mixed layer or across the mixed layer base to the ocean interior. We find that the increase in anthropogenic CO_2 uptake is almost entirely compensated by the subduction of DIC_{anth} across the mixed layer base (+0.02 PgC/year^{-2} compared to 0.015 PgC/year^{-2} for the

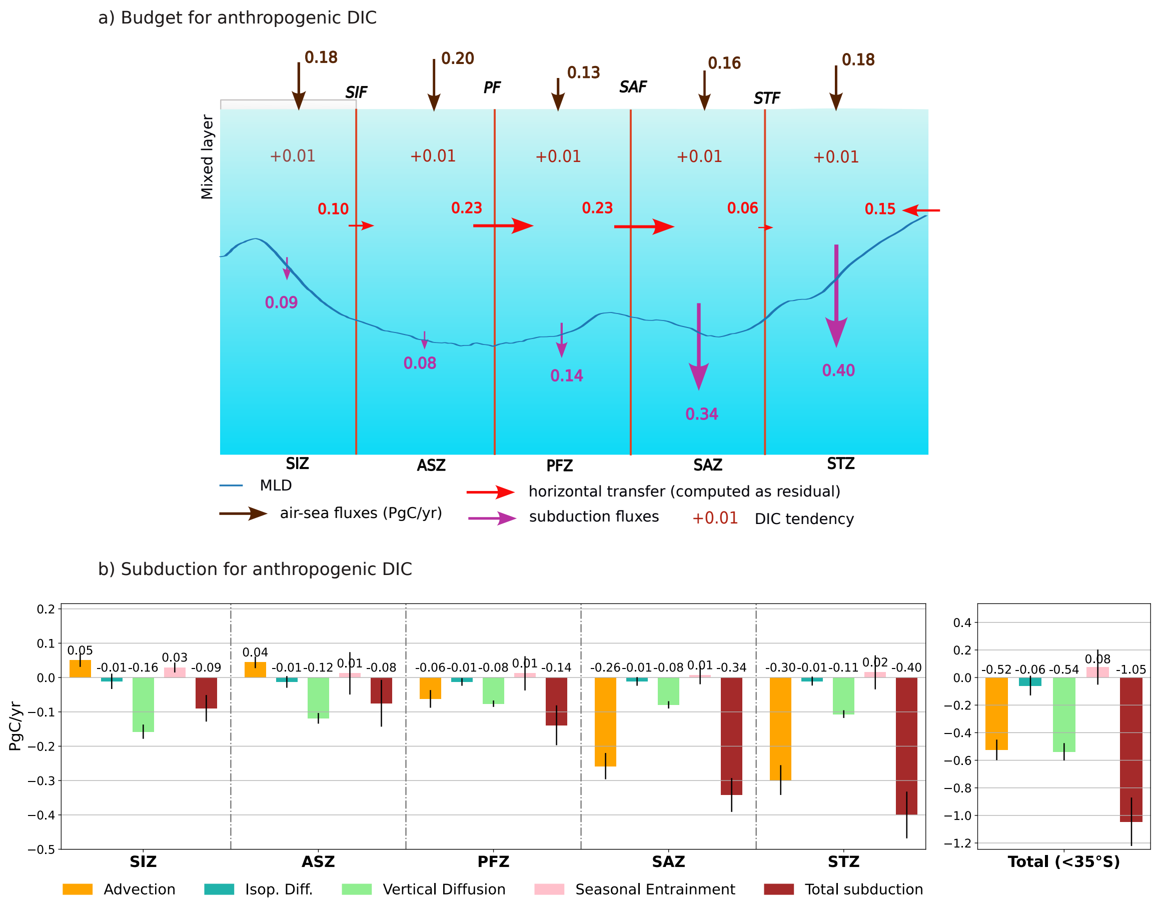

Figure 6. Same as Figure 5 but for DIC_{ant} except for air-sea fluxes which use the same scale as the other fluxes here.

air-sea fluxes). In our model, the subduction rate of DIC_{anth} thus adjusts to the increase in the uptake of anthropogenic CO_2 over a 20-year period, in line with Bopp et al. (2015).

3.2.2 Physical drivers of the subduction

When averaged over the SO, subduction of DIC_{anth} is mainly achieved through vertical diffusion and advection, which each contribute to about half of the total flux of anthropogenic carbon towards the ocean interior (Fig. 6b). While advective fluxes dominate north of the ACC, accounting for 69% of the anthropogenic DIC transferred across the mixed layer base (with respect to the sum of all in and out fluxes north of the SAF), vertical diffusion dominates south of the SAF, accounting for 62% of this transfer. As expected, advection brings anthropogenic carbon within the mixed layer in the southernmost regions (SIZ, ASZ) due to the large-scale upwelling, and transfers carbon into the ocean interior in the northernmost regions (SAZ, STZ) through downwelling. In contrast, vertical diffusion acts to transfer anthropogenic carbon below the mixed layer in all regions due to the large-scale upward vertical gradient of DIC_{anth}.

The predominance of vertical diffusion south of the PF arises from the strong positive gradient of anthropogenic DIC across the mixed layer base, due to the presence of DIC_{anth}-depleted CDW just below the mixed layer. Seasonal entrainment is opposed to the gradient of DIC_{anth} and brings carbon back into the mixed layer, accounting for 7% of the sum of all fluxes on a yearly average. This small net contribution however results from larger and both positive and negative contributions of seasonal entrainment to the transfer of carbon across the mixed layer base across years. Isopycnal diffusion works to transfer DIC_{anth} to the ocean interior, as a result from the vertical gradient of DIC_{anth}, and is almost negligible, representing only 5% of the total transfer over the SO.

The seasonality of vertical diffusion of DIC_{anth} is strongest in the SIZ, with a very large subduction at the end of the summer (Fig. S7.b). A possible explanation for this signal is the accumulation of DIC_{anth} in the mixed layer over the summer and therefore a maximum vertical gradient around March. The vertical diffusion coefficient must also be larger in summer in the SIZ, when sea ice cover reaches its minimum extent and winds can impact the upper layer of the ocean. The other regions show larger subduction at the end of winter, following the largest seasonal uptake driven by high solubility, and energy input by the winds.

3.3 Spatial distribution of the subduction fluxes

For both the total and anthropogenic DIC, the physical transfer across the mixed layer base is mainly driven by the same processes, the advection and the vertical diffusion (see Sections 3.1 and 3.2). Both processes generally drive an enhanced transfer of DIC across the mixed layer base within western boundary currents, and in the PFZ of the Atlantic and Pacific sectors, as well as in the wake of the Kerguelen Plateau and Macquarie Ridge (Fig. 7). However, advection is the process that dominates the spatial pattern of the subduction fluxes for both total and anthropogenic DIC given that locally the magnitude of advective fluxes is several order of magnitude larger than that of diffusive fluxes.

The spatial distribution of advective fluxes is characterized by locally alternating intense obduction and subduction of DIC which, once integrated over large regions such as the interfrontal zones, cancel out to give contributions of magnitude comparable to diffusive fluxes. These alternating patterns arise from the lateral induction, that is from the interaction between the mean flow and the sloped mixed layer base, that locally creates either export or import of DIC out or into the mixed layer. The contribution of the vertical advection remains generally one order of magnitude smaller than the lateral component even locally (not shown). Enhanced contribution of advection can thus be found where the mixed layer base is steep and the flow is intense which is typical of western boundary currents (intense flow), and the northern ACC (PFZ and SAZ where mixed layer base is sloped; Fig. 7). More locally, enhanced advective fluxes across the mixed layer base are found within the ACC around major bathymetric obstacles such as the Kerguelen and Campbell Plateaus and the Drake Passage (Fig. 8), that is where the jets of the ACC accelerate and meander. As the flow circumvents these obstacles, carbon is either obducted then subducted, or the other way round, depending on the meridional gradient of the mixed layer depth. For instance, upstream of Drake Passage, subduction occurs as the flow heads northward away from the deep mixed layers of the southeast Pacific, while downstream, obduction occurs as the flow encounters gradually deeper mixed layers (Figs. 2, 7 and 8). These localized enhanced subduction fluxes at bathymetric obstacles, which are associated with increased mesoscale activity, are corroborated by observational evidence (Dove et al., 2021; Sallée et al., 2012).

4 Discussion

The analyses of physical processes driving the transfer of DIC across the base of the mixed layer reveal that, in our model, advection is predominant over the SO for both the total and anthropogenic components. This result is in good agreement with recent estimates made from BGC-Argo floats measurements which shows that advection across the mixed layer is the main process by which DIC_{tot} enters the mixed layer of the SIZ and ASZ (J. Sauvé, personnal communication). This important role of advection in DIC subduction also aligns with the findings of previous modelling studies but, importantly, it is reinforced in our model. Using a similar model configuration as ours but at a coarser resolution, Levy et al. (2013) found a transfer of 14.3 PgC/year towards the ocean interior south of 44°S, against 22.8 PgC/year in our study. The larger obduction in our model is mostly due to the advection term which is almost twice the magnitude of that found in Levy et al. (2013) (∼20 PgC/year against ∼12 PgC/year). As resolution is increased, a more vigorous physical circulation is resolved resulting in larger advective fluxes. Locally, these fluxes can be almost one order of magnitude larger in an eddying model (0.25°) than in a non-eddying model (2°; not shown). Yet, 0.25° resolution is only eddy-permitting so that smaller mesoscale and submesoscale features are not resolved in the model. These mesoscale and submesoscale processes are known to have a non-negligible impact on tracer transport, especially at the mixed layer (Calvert et al., 2020; Balwada et al., 2018; Fox-Kemper & Ferrari, 2008). Previous studies hence suggest an even stronger role of advection when further refining the resolution.

The only region where the predominance of advection is challenged is south of the ACC within the SIZ and ASZ where vertical diffusion contributes equally to the transfer of DIC_{anth} across the mixed layer base as advection (Section 3.2). The important role of vertical diffusion in transferring carbon across the mixed layer is also pointed out in observation-based studies (Sauvé et al., 2023). Yet, the poorly known diffusivity coefficients translate into large uncertainties in the contribution of the vertical diffusion for observational estimates as well as for models. Interestingly, when integrated south of 44°S, that is when we move the boundary of the SO by 9° to the south, the contribution of vertical diffusion is found to largely dominate that of advection (0.42 PgC/year for vertical diffusion compared to around 0.05 PgC/year for advection). The decreased contribution from the advective term is due to the strong compensation between the positive contribution (obduction) south of the ACC and the negative contribution (subduction) north of the ACC (Fig. 6b). Moving the boundary of the SO further south thus removes the strong subduction occurring in the STZ and part of the SAZ. This predominance of vertical diffusion in transferring DIC_{ant} across the mixed layer base south of 44°S corroborates the results of Bopp et al. (2015) who found a subduction rate by vertical mixing (combining vertical diffusion, seasonal entrainment and isopycnal diffusion) of 0.69 PgC/year for 1998-2007 (compared to 0.40 PgC/year in our study but for 1995-2014) in their 2° resolution NEMO-PISCES model using the same online diagnostic as in the present study. Vertical diffusion fluxes in our study are weaker than in lower resolution

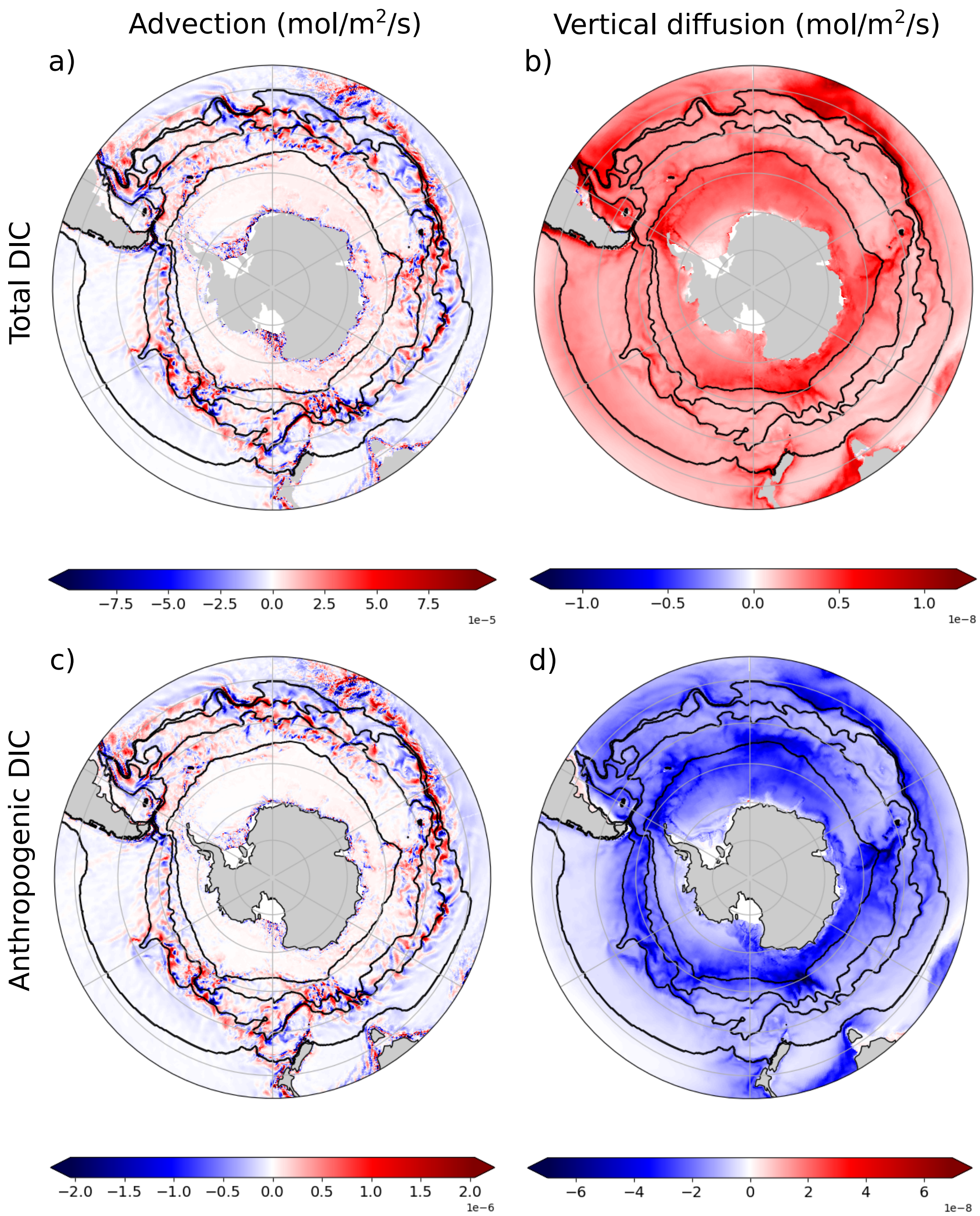

Figure 7. Map of the two dominant processes contributing to the subduction of DIC across the mixed layer base: (a,c) advection and (b,d) vertical diffusion of (a,c) DIC$_{tot}$ and (b,d) DIC$_{anth}$ averaged over 1995-2014. Positive fluxes correspond to obduction. Black contours correspond to the boundaries between the five zones. Note the different scales used across the panels to help the visualization of the spatial patterns.

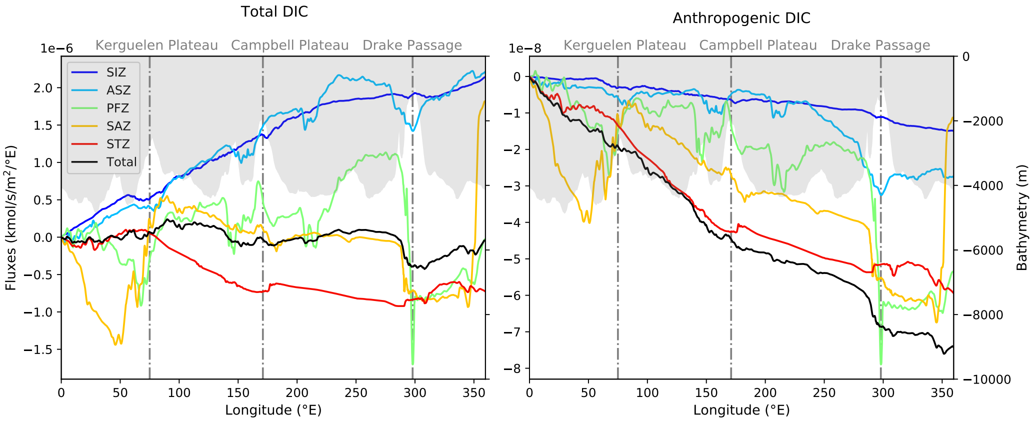

Figure 8. 1995-2014 averaged transfer of DIC across the base of the mixed layer cumulatively summed along latitude within each region (colored lines) and the SO (black line) for (a) the total and (b) the anthropogenic carbon component. Positive values correspond to obduction. Bathymetry is shown in the background in white with the major bathymetric features indicated using vertical dashed-dotted lines.

simulations. Overall, these comparisons of subduction fluxes integrated between different SO domains highlight the strong dependency of subduction estimates to the region studied. The five regions bounded by fronts that are used in this study thus provide a physically coherent framework to investigate the fluxes and perform inter-comparisons between models and evaluation against observations.

Within these coherent regions, subduction fluxes show large spatial variations (Fig. 7a,c). This is in particular the case of advection which can successively import and export carbon in and out of the mixed layer over relatively short distances (Fig. 7). These alternating bands of subduction and obduction result from the interaction between the flow and the spatial variations of the mixed layer depth. While similar bands can be detected in observations (Chen & Schofield, 2024; Sallée et al., 2012) and in coarser resolution models (not shown), their extent considerably reduces with resolution. The very localized nature of these advection fluxes poses a challenge to estimating subduction rates of carbon from observations. Though more homogeneous in their spatial pattern, vertical diffusive fluxes might also be subject to strong spatial variations that neither models nor observations are currently able to capture through the turbulent mixing parameterizations.

5 Conclusion

In this study, we used an eddying global ocean model to compute budgets of DIC within the mixed layer of the Southern Ocean (south of 35°S) and associated fluxes across the base of the mixed layer over 1995-2014. Two simulations with the same circulation but different atmospheric CO_2 concentrations were used to contrast the total and anthropogenic DIC budgets and fluxes and to investigate the physical processes driving them within five physically consistent regions of the Southern Ocean. We found that:

1. In the Southern Ocean, 11.24 PgC/year of total DIC is obducted into the mixed layer and 1.05 PgC/year of anthropogenic DIC is subducted into the ocean interior over 1995-2014. No net accumulation nor loss of total or anthropogenic DIC is found within the mixed layer over the 20 years investigated, the uptake of an-

thropogenic CO_2 being largely compensated by the subduction towards the ocean interior.

2. South of the Subantarctic Front (SAF), DIC is obducted into the mixed layer predominantly through advection before being transported northward across the SAF. North of the SAF, DIC is subducted towards the ocean interior, with partial compensation by vertical diffusion. In the Subtropical Zone (STZ), 6.53 PgC/year of total DIC is transported to lower latitudes within the mixed layer. Advection is the main process driving the transfer of total DIC across the base of the mixed layer in all regions, the contribution by vertical diffusion being only a third of that of advection over the Southern Ocean.
3. Anthropogenic CO_2 is taken up in similar amounts in all regions of the SO. The anthropogenic CO_2 absorbed south of the SAF is transferred towards the north and subducted north of SAF together with the anthropogenic CO_2 absorbed in the SAZ and STZ. Advection and vertical diffusion equally contribute to the transfer of anthropogenic DIC across the mixed layer base south of 35°S. While vertical diffusion dominates south of the PF, advection is the main driver of subduction north of the SAF.
4. The transfer of DIC across the mixed layer base via vertical diffusion is enhanced near the Sea Ice Front (SIF) and within boundary currents, in particular in the Indian and Atlantic sectors. Advective fluxes are intensified within the ACC fronts and the boundary currents. Importantly, these advective fluxes are very localized and strengthen near major topographic features.

Overall, our results point to an important and localized role of advective fluxes in transferring carbon to the ocean interior thus calling for accurate and high sampling measurements of the flow and estimates of mixed layer depth. Despite the predominant role of advection, vertical diffusion remains an important player in transferring carbon across the mixed layer which implies better constraining the eddy diffusivity coefficients through additional measurements. Moreover, a thorough assessment of carbon sequestration rates and of the underlying processes requires to include organic carbon in the mixed layer budget and in the analyses of subduction fluxes. This investigation is left to a future study.

Acknowledgments

SLC was supported by the Natural Sciences and Engineering Research Council of Canada (NSERC) through the Discovery grant (RGPIN/2018-04985) awarded to C.O.D. and by the Québec Océan strategic cluster. The simulations used in this study were run by Christian Ethé with computational resources from TGCC in the ESPRI (Ensemble de Services Pour la Recherche l'IPSL) computing and data center (`https://mesocentre.ipsl.fr`).We thank Seth Bushinsky and Jade Sauvé for sharing their data with us. We also thank Olivier Torres and Manon Berger who helped process and transfer the model output used in this study.

6 Data Availability Statement

The model outputs and code used in this study are available with this private link to the project zenodo draft: `https://zenodo.org/records/14057544?preview=1&token=eyJhbGciOiJIUzUxMiJ9.eyJpZCI6ImJhN2E5ZWYyLWQ5YWQtNGE2Ni04YWE0LTU2ZmRiYmE3YmI3OSIsImRhdGEiOnt9LC.Khfb8Dntq-p45Ebe-5eaHF0_n407F6VdBXmJdROtXou0hDlq2AuoqaF9-PCQV-IdnmqJxV7w-4Q4tjZ_nHivqA`. This zenodo repository will be made publicly available as specified in the data and software guidance. Observational datasets used in this study are available online, with temperature and salinity from CORA5.2 at `https://data.marine.copernicus.eu/product/INSITU_GLO_PHY_TS_OA_MY_013_052/` (Szekely et al., 2019), DIC from GLODAPv2 at `doi:10.3334/CDIAC/OTG.NDP093_GLODAPv2` (Lauvset et al., 2016), and MLD from `http://www.jamstec.go.jp/ARGO/J_ARGOe.html` (Hosoda et al., 2010). The air-sea fluxes values from Bushinsky et al. (2019) were given by the corresponding author of this article after a personal request.

References

Adcroft, A., Anderson, W., Balaji, V., Blanton, C., Bushuk, M., Dufour, C. O., ... Zhang, R. (2019, October). The GFDL Global Ocean and Sea Ice Model OM4.0: Model Description and Simulation Features. *Journal of Advances in Modeling Earth Systems*, *11*(10), 3167–3211. doi: 10.1029/2019MS001726

Aumont, O., Ethé, C., Tagliabue, A., Bopp, L., & Gehlen, M. (2015, August). PISCES-v2: an ocean biogeochemical model for carbon and ecosystem studies. *Geoscientific Model Development*, *8*(8), 2465–2513. doi: 10.5194/gmd-8-2465-2015

Bakker, D. C. E., Pfeil, B., Landa, C. S., Metzl, N., O'Brien, K. M., Olsen, A., ... Xu, S. (2016, September). A multi-decade record of high-quality CO2 data in version 3 of the Surface Ocean CO2 Atlas (SOCAT). *Earth System Science Data*, *8*(2), 383–413. doi: 10.5194/essd-8-383-2016

Balwada, D., Smith, K. S., & Abernathey, R. (2018, September). Submesoscale Vertical Velocities Enhance Tracer Subduction in an Idealized Antarctic Circumpolar Current. *Geophysical Research Letters*, *45*(18), 9790–9802. doi: 10.1029/2018GL079244

Blanke, B., & Delecluse, P. (1993). Variability of the Tropical Atlantic Ocean Simulated by a General Circulation Model with Two Different Mixed-Layer Physics. *Journal of Physical Oceanography*, *23*, 1363–1388.

Bopp, L., Lévy, M., Resplandy, L., & Sallée, J. B. (2015, August). Pathways of anthropogenic carbon subduction in the global ocean. *Geophysical Research Letters*, *42*(15), 6416–6423. doi: 10.1002/2015GL065073

Bourgeois, T., Goris, N., Schwinger, J., & Tjiputra, J. F. (2022, January). Stratification constrains future heat and carbon uptake in the Southern Ocean between 30°S and 55°S. *Nature Communications*, *13*(1), 340. doi: 10.1038/s41467-022-27979-5

Brady, R. X., Maltrud, M. E., Wolfram, P. J., Drake, H. F., & Lovenduski, N. S. (2021, October). The Influence of Ocean Topography on the Upwelling of Carbon in the Southern Ocean. *Geophysical Research Letters*, *48*(19). doi: 10.1029/2021GL095088

Bushinsky, S. M., Landschützer, P., Rödenbeck, C., Gray, A. R., Baker, D., Mazloff, M. R., ... Sarmiento, J. L. (2019, November). Reassessing Southern Ocean Air-Sea CO_2 Flux Estimates With the Addition of Biogeochemical Float Observations. *Global Biogeochemical Cycles*, *33*(11), 1370–1388. doi: 10.1029/2019GB006176

Calvert, D., Nurser, G., Bell, M. J., & Fox-Kemper, B. (2020, October). The impact of a parameterisation of submesoscale mixed layer eddies on mixed layer depths in the NEMO ocean model. *Ocean Modelling*, *154*, 101678. doi: 10.1016/j.ocemod.2020.101678

Carroll, D., Menemenlis, D., Dutkiewicz, S., Lauderdale, J. M., Adkins, J. F., Bowman, K. W., ... Zhang, H. (2022, March). Attribution of Space-Time Variability in Global-Ocean Dissolved Inorganic Carbon. *Global Biogeochemical Cycles*, *36*(3). doi: 10.1029/2021GB007162

Chen, M. L., & Schofield, O. (2024, October). Spatial and Seasonal Controls on Eddy Subduction in the Southern Ocean. *Geophysical Research Letters*, *51*(20), e2024GL109246. doi: 10.1029/2024GL109246

Davila, X., Gebbie, G., Brakstad, A., Lauvset, S. K., McDonagh, E. L., Schwinger, J., & Olsen, A. (2022, May). How Is the Ocean Anthropogenic Carbon Reservoir Filled? *Global Biogeochemical Cycles*, *36*(5), e2021GB007055. doi:

10.1029/2021GB007055

de Boyer Montégut, C. (2004). Mixed layer depth over the global ocean: An examination of profile data and a profile-based climatology. *Journal of Geophysical Research*, *109*(C12), C12003. doi: 10.1029/2004JC002378

DeVries, T. (2014, July). The oceanic anthropogenic CO $_2$ sink: Storage, air-sea fluxes, and transports over the industrial era. *Global Biogeochemical Cycles*, *28*(7), 631–647. doi: 10.1002/2013GB004739

DeVries, T., Holzer, M., & Primeau, F. (2017, February). Recent increase in oceanic carbon uptake driven by weaker upper-ocean overturning. *Nature*, *542*(7640), 215–218. doi: 10.1038/nature21068

Doney, S. C., Lindsay, K., Caldeira, K., Campin, J.-M., Drange, H., Dutay, J.-C., … Yool, A. (2004, September). Evaluating global ocean carbon models: The importance of realistic physics. *Global Biogeochemical Cycles*, *18*(3), n/a–n/a. doi: 10.1029/2003GB002150

Dove, L. A., Thompson, A. F., Balwada, D., & Gray, A. R. (2021, July). Observational Evidence of Ventilation Hotspots in the Southern Ocean. *Journal of Geophysical Research: Oceans*, *126*(7). doi: 10.1029/2021JC017178

Drake, H. F., Morrison, A. K., Griffies, S. M., Sarmiento, J. L., Weijer, W., & Gray, A. R. (2018, January). Lagrangian Timescales of Southern Ocean Upwelling in a Hierarchy of Model Resolutions. *Geophysical Research Letters*, *45*(2), 891–898. doi: 10.1002/2017GL076045

Dufour, C. O., Griffies, S. M., de Souza, G. F., Frenger, I., Morrison, A. K., Palter, J. B., … Slater, R. D. (2015, December). Role of Mesoscale Eddies in Cross-Frontal Transport of Heat and Biogeochemical Tracers in the Southern Ocean. *Journal of Physical Oceanography*, *45*(12), 3057–3081. doi: 10.1175/JPO-D-14-0240.1

Dufour, C. O., Le Sommer, J., Zika, J. D., Gehlen, M., Orr, J. C., Mathiot, P., & Barnier, B. (2012, October). Standing and Transient Eddies in the Response of the Southern Ocean Meridional Overturning to the Southern Annular Mode. *Journal of Climate*, *25*(20), 6958–6974. doi: 10.1175/JCLI-D-11-00309.1

Dufour, C. O., Sommer, J. L., Gehlen, M., Orr, J. C., Molines, J., Simeon, J., & Barnier, B. (2013, September). Eddy compensation and controls of the enhanced sea-to-air CO_2 flux during positive phases of the Southern Annular Mode. *Global Biogeochemical Cycles*, *27*(3), 950–961. doi: 10.1002/gbc.20090

Dussin, R., Barnier, B., Brodeau, L., & Molines, J.-M. (2016). *The Making Of the DRAKKAR FORCING SET DFS5.* DRAKKAR/MyOcean Report.

Fox-Kemper, B., & Ferrari, R. (2008, June). Parameterization of Mixed Layer Eddies. Part II: Prognosis and Impact. *Journal of Physical Oceanography*, *38*(6), 1166–1179. doi: 10.1175/2007JPO3788.1

Friedlingstein, P., O'Sullivan, M., & Jones, M. W. (2020, December). Global Carbon Budget 2020. *Earth System Science Data*, *12*(4), 3269–3340. doi: 10.5194/essd-12-3269-2020

Frölicher, T. L., Sarmiento, J. L., Paynter, D. J., Dunne, J. P., Krasting, J. P., & Winton, M. (2015, January). Dominance of the Southern Ocean in Anthropogenic Carbon and Heat Uptake in CMIP5 Models. *Journal of Climate*, *28*(2), 862–886. doi: 10.1175/JCLI-D-14-00117.1

Gent, P., & McWilliams, J. (1990). Isopycnal Mixing in Ocean Circulation Models. *Journal of Physical Oceanography*, *20*, 150–155. doi: https://doi.org/10.1175/1520-0485(1990)020⟨0150:IMIOCM⟩2.0.CO;2

Gent, P., McWilliams, J., Willebrand, J., & McDougall, T. J. (1995). Parameterizing Eddy-Induced Tracer Transports in Ocean Circulation Models. *Journal of Physical Oceanography*, *25*(4), 463–474.

Graven, H. D., Gruber, N., Key, R., Khatiwala, S., & Giraud, X. (2012, October). Changing controls on oceanic radiocarbon: New insights on shallow-to-deep ocean exchange and anthropogenic CO $_2$ uptake: CHANGING CONTROLS

ON OCEANIC ^{14}C. *Journal of Geophysical Research: Oceans*, *117*(C10), n/a–n/a. doi: 10.1029/2012JC008074

Gray, A. R., Johnson, K. S., Bushinsky, S. M., Riser, S. C., Russell, J. L., Talley, L. D., ... Sarmiento, J. L. (2018, September). Autonomous Biogeochemical Floats Detect Significant Carbon Dioxide Outgassing in the High-Latitude Southern Ocean. *Geophysical Research Letters*, *45*(17), 9049–9057. doi: 10.1029/2018GL078013

Gruber, N., Landschützer, P., & Lovenduski, N. S. (2019). The Variable Southern Ocean Carbon Sink. *Annual Review of Marine Science*, *11*(1), 159–186. (_eprint: https://doi.org/10.1146/annurev-marine-121916-063407) doi: 10.1146/annurev-marine-121916-063407

Hallberg, R. (2013, December). Using a resolution function to regulate parameterizations of oceanic mesoscale eddy effects. *Ocean Modelling*, *72*, 92–103. doi: 10.1016/j.ocemod.2013.08.007

Hallberg, R., & Gnanadesikan, A. (2006, December). The Role of Eddies in Determining the Structure and Response of the Wind-Driven Southern Hemisphere Overturning: Results from the Modeling Eddies in the Southern Ocean (MESO) Project. *Journal of Physical Oceanography*, *36*(12), 2232–2252. doi: 10.1175/JPO2980.1

Hauck, J., Gregor, L., Nissen, C., Patara, L., Hague, M., Mongwe, P., ... Terhaar, J. (2023, November). The Southern Ocean Carbon Cycle 1985–2018: Mean, Seasonal Cycle, Trends, and Storage. *Global Biogeochemical Cycles*, *37*(11), e2023GB007848. doi: 10.1029/2023GB007848

Hauck, J., Zeising, M., Le Quéré, C., Gruber, N., Bakker, D. C. E., Bopp, L., ... Séférian, R. (2020, October). Consistency and Challenges in the Ocean Carbon Sink Estimate for the Global Carbon Budget. *Frontiers in Marine Science*, *7*, 571720. doi: 10.3389/fmars.2020.571720

Hong, Y., Du, Y., Xia, X., Xu, L., Zhang, Y., & Xie, S.-P. (2021, September). Subantarctic Mode Water and its long-term change in CMIP6 models. *Journal of Climate*, 1–51. doi: 10.1175/JCLI-D-21-0133.1

Hosoda, S., Ohira, T., Sato, K., & Suga, T. (2010, December). Improved description of global mixed-layer depth using Argo profiling floats. *Journal of Oceanography*, *66*(6), 773–787. doi: 10.1007/s10872-010-0063-3

Iudicone, D., Rodgers, K. B., Stendardo, I., Aumont, O., Madec, G., Bopp, L., ... Ribera d'Alcala', M. (2011, May). Water masses as a unifying framework for understanding the Southern Ocean Carbon Cycle. *Biogeosciences*, *8*(5), 1031–1052. doi: 10.5194/bg-8-1031-2011

Karleskind, P., Lévy, M., & Memery, L. (2011, February). Subduction of carbon, nitrogen, and oxygen in the northeast Atlantic. *Journal of Geophysical Research*, *116*(C2), C02025. doi: 10.1029/2010JC006446

Lachkar, Z., Orr, J. C., Dutay, J.-C., & Delecluse, P. (2007, October). Effects of mesoscale eddies on global ocean distributions of CFC-11, CO2 and \Delta 14C. *Ocean Science*, *3*(4), 461–482. doi: 10.5194/os-3-461-2007

Landschützer, P., Gruber, N., & Bakker, D. C. E. (2016, October). Decadal variations and trends of the global ocean carbon sink. *Global Biogeochemical Cycles*, *30*(10), 1396–1417. doi: 10.1002/2015GB005359

Landschützer, P., Gruber, N., Bakker, D. C. E., Schuster, U., Nakaoka, S., Payne, M. R., ... Zeng, J. (2013, November). A neural network-based estimate of the seasonal to inter-annual variability of the Atlantic Ocean carbon sink. *Biogeosciences*, *10*(11), 7793–7815. doi: 10.5194/bg-10-7793-2013

Landschützer, P., Laruelle, G. G., Roobaert, A., & Regnier, P. (2020, October). A uniform pCO_2 climatology combining open and coastal oceans. *Earth System Science Data*, *12*(4), 2537–2553. doi: 10.5194/essd-12-2537-2020

Lauvset, S. K., Key, R. M., Olsen, A., van Heuven, S., Velo, A., Lin, X., ... Watelet, S. (2016). A new global interior ocean mapped climatology: the

1°x1° GLODAP version 2. *Earth System Science Data*, *8*(2), 325–340. doi: 10.5194/essd-8-325-2016

Levy, M., Bopp, L., Karleskind, P., Resplandy, L., Ethe, C., & Pinsard, F. (2013, December). Physical pathways for carbon transfers between the surface mixed layer and the ocean interior. *Global Biogeochemical Cycles*, *27*(4), 1001–1012. doi: 10.1002/gbc.20092

Li, Z., England, M. H., Groeskamp, S., Cerovečki, I., & Luo, Y. (2021, July). The Origin and Fate of Subantarctic Mode Water in the Southern Ocean. *Journal of Physical Oceanography*. doi: 10.1175/JPO-D-20-0174.1

Locarnini, R. A., Mishonov, A. V., Antonov, J. I., Boyer, T. P., Garcia, H. E., Baranova, O. K., … Seidov, D. (2013, September). *World ocean atlas 2013. Volume 1, Temperature.* (Publisher: U.S. Department of Commerce, National Oceanic and Atmospheric Administration, National Environmental Satellite, Data and Information Service) doi: 10.7289/V55X26VD

Lumpkin, R., & Speer, K. (2007, October). Global Ocean Meridional Overturning. *Journal of Physical Oceanography*, *37*(10), 2550–2562. doi: 10.1175/JPO3130.1

Madec, G. (2008). NEMO ocean engine. *Institut Pierre-Simon Laplace (IPSL)*. (Publisher: Zenodo) doi: 10.5281/zenodo.3878122

Madec, G., Delécluse, P., Imbard, M., & Lévy, C. (1998). OPA 8.1 Ocean General Circulation Model reference manual. *Notes du pôle de mode´lisation, laboratoire d'océanographie dynamique et de climatologie, Institut Pierre Simon Laplace des sciences de l'environnement global*, *11*.

Madec, G., & the NEMO Team. (2016). *NEMO ocean engine - Note du Pôle de modélisation de l'Institut Pierre-Simon Laplace No 27.*

Marshall, J., & Speer, K. (2012, March). Closure of the meridional overturning circulation through Southern Ocean upwelling. *Nature Geoscience*, *5*(3), 171–180. doi: 10.1038/ngeo1391

Mathiot, P., Jenkins, A., Harris, C., & Madec, G. (2017, July). Explicit representation and parametrised impacts of under ice shelf seas in the z* coordinate ocean model NEMO 3.6. *Geoscientific Model Development*, *10*(7), 2849–2874. doi: 10.5194/gmd-10-2849-2017

Maurer, T. L., Plant, J. N., & Johnson, K. S. (2021, February). *Delayed-mode quality control of oxygen, nitrate and pH data on SOCCOM biogeochemical profiling floats* (preprint). Oceanography. doi: 10.1002/essoar.10506241.1

Mikaloff Fletcher, S. E., Gruber, N., Jacobson, A. R., Doney, S. C., Dutkiewicz, S., Gerber, M., … Sarmiento, J. L. (2006, June). Inverse estimates of anthropogenic CO_2 uptake, transport, and storage by the ocean. *Global Biogeochemical Cycles*, *20*(2), n/a–n/a. doi: 10.1029/2005GB002530

Mikaloff Fletcher, S. E., Gruber, N., Jacobson, A. R., Gloor, M., Doney, S. C., Dutkiewicz, S., … Sarmiento, J. L. (2007, March). Inverse estimates of the oceanic sources and sinks of natural CO_2 and the implied oceanic carbon transport. *Global Biogeochemical Cycles*, *21*(1). doi: 10.1029/2006GB002751

Olsen, A., Key, R. M., van Heuven, S., Lauvset, S. K., Velo, A., Lin, X., … Suzuki, T. (2016, August). The Global Ocean Data Analysis Project version 2 (GLODAPv2) – an internallyconsistent data product for the world ocean. *Earth System Science Data*, *8*(2), 297–323. doi: 10.5194/essd-8-297-2016

Orr, J. C., Maier-Reimer, E., Mikolajewicz, U., Monfray, P., Sarmiento, J. L., Toggweiler, J. R., … Boutin, J. (2001, March). Estimates of anthropogenic carbon uptake from four three-dimensional global ocean models. *Global Biogeochemical Cycles*, *15*(1), 43–60. doi: 10.1029/2000GB001273

Orr, J. C., Najjar, R. G., Aumont, O., Bopp, L., Bullister, J. L., Danabasoglu, G., … Yool, A. (2017, June). Biogeochemical protocols and diagnostics for the CMIP6 Ocean Model Intercomparison Project (OMIP). *Geoscientific Model Development*, *10*(6), 2169–2199. doi: 10.5194/gmd-10-2169-2017

Orsi, A. H., Whitworth, T., & Nowlin, W. D. (1995, May). On the meridional extent and fronts of the Antarctic Circumpolar Current. *Deep Sea Research Part I: Oceanographic Research Papers*, *42*(5), 641–673. doi: 10.1016/0967-0637(95)00021-W

Park, Y.-H., Charriaud, E., & Fieux, M. (1998, November). Thermohaline structure of the Antarctic Surface Water/Winter Water in the Indian sector of the Southern Ocean. *Journal of Marine Systems*, *17*(1-4), 5–23. doi: 10.1016/S0924-7963(98)00026-8

Planchat, A., Kwiatkowski, L., Bopp, L., Torres, O., Christian, J. R., Butenschön, M., … Stock, C. (2023, April). The representation of alkalinity and the carbonate pump from CMIP5 to CMIP6 Earth system models and implications for the carbon cycle. *Biogeosciences*, *20*(7), 1195–1257. doi: 10.5194/bg-20-1195-2023

Redi, M. H. (1982). Oceanic Isopycnal Mixing by Coordinate Rotation. *Journal of Physical Oceanography*, *12*(10), 1154–1158.

Rodgers, K. B., Aumont, O., Mikaloff Fletcher, S. E., Plancherel, Y., Bopp, L., De Boyer Montégut, C., … Wanninkhof, R. (2014, August). Strong sensitivity of Southern Ocean carbon uptake and nutrient cycling to wind stirring. *Biogeosciences*, *11*(15), 4077–4098. doi: 10.5194/bg-11-4077-2014

Sabine, C. L. (2004, July). The Oceanic Sink for Anthropogenic CO2. *Science*, *305*(5682), 367–371. doi: 10.1126/science.1097403

Sallée, J.-B., Matear, R. J., Rintoul, S. R., & Lenton, A. (2012, August). Localized subduction of anthropogenic carbon dioxide in the Southern Hemisphere oceans. *Nature Geoscience*, *5*(8), 579–584. doi: 10.1038/ngeo1523

Sarmiento, J. L., Orr, J. C., & Siegenthaler, U. (1992). A perturbation simulation of CO_2 uptake in an ocean general circulation model. *Journal of Geophysical Research*, *97*(C3), 3621. doi: 10.1029/91JC02849

Sauvé, J., Gray, A. R., Prend, C. J., Bushinsky, S. M., & Riser, S. C. (2023, November). Carbon Outgassing in the Antarctic Circumpolar Current Is Supported by Ekman Transport From the Sea Ice Zone in an Observation-Based Seasonal Mixed-Layer Budget. *Journal of Geophysical Research: Oceans*, *128*(11), e2023JC019815. doi: 10.1029/2023JC019815

Szekely, T., Gourrion, J., Pouliquen, S., & Reverdin, G. (2019, December). The CORA 5.2 dataset for global in situ temperature and salinity measurements: data description and validation. *Ocean Science*, *15*(6), 1601–1614. doi: 10.5194/os-15-1601-2019

Talley, L. D. (2013, March). Closure of the Global Overturning Circulation Through the Indian, Pacific, and Southern Oceans: Schematics and Transports. *Oceanography*, *26*(1), 80–97.

Tamsitt, V., Drake, H. F., Morrison, A. K., Talley, L. D., Dufour, C. O., Gray, A. R., … Weijer, W. (2017, December). Spiraling pathways of global deep waters to the surface of the Southern Ocean. *Nature Communications*, *8*(1), 172. doi: 10.1038/s41467-017-00197-0

Terhaar, J., Frölicher, T. L., & Joos, F. (2021, April). Southern Ocean anthropogenic carbon sink constrained by sea surface salinity. *Science Advances*, *7*(18), eabd5964. doi: 10.1126/sciadv.abd5964

Terhaar, J., Goris, N., Müller, J. D., DeVries, T., Gruber, N., Hauck, J., … Séférian, R. (2024, March). Assessment of Global Ocean Biogeochemistry Models for Ocean Carbon Sink Estimates in RECCAP2 and Recommendations for Future Studies. *Journal of Advances in Modeling Earth Systems*, *16*(3), e2023MS003840. doi: 10.1029/2023MS003840

Terhaar, J., Orr, J. C., Gehlen, M., Ethé, C., & Bopp, L. (2019, June). Model constraints on the anthropogenic carbon budget of the Arctic Ocean. *Biogeosciences*, *16*(11), 2343–2367. doi: 10.5194/bg-16-2343-2019

Toyama, K., Rodgers, K. B., Blanke, B., Iudicone, D., Ishii, M., Aumont, O., &

Sarmiento, J. L. (2017, November). Large Reemergence of Anthropogenic Carbon into the Ocean's Surface Mixed Layer Sustained by the Ocean's Overturning Circulation. *Journal of Climate*, *30*(21), 8615–8631. doi: 10.1175/JCLI-D-16-0725.1

Vancoppenolle, M., Fichefet, T., & Goosse, H. (2009, January). Simulating the mass balance and salinity of Arctic and Antarctic sea ice. 2. Importance of sea ice salinity variations. *Ocean Modelling*, *27*(1-2), 54–69. doi: 10.1016/j.ocemod.2008.11.003

Wanninkhof, R. (1992). Relationship between wind speed and gas exchange over the ocean. *Journal of Geophysical Research*, *97*(C5), 7373. doi: 10.1029/92JC00188

Williams, N. L., Juranek, L. W., Feely, R. A., Johnson, K. S., Sarmiento, J. L., Talley, L. D., ... Takeshita, Y. (2017, March). Calculating surface ocean pCO $_2$ from biogeochemical Argo floats equipped with pH: An uncertainty analysis: Calculating Ocean pCO $_2$ From Float pH. *Global Biogeochemical Cycles*, *31*(3), 591–604. doi: 10.1002/2016GB005541

Zweng, M. M., Reagan, J. R., Antonov, J. I., Locarnini, R. A., Mishonov, A. V., Boyer, T. P., ... Biddle, M. M. (2013, September). *World ocean atlas 2013. Volume 2, Salinity.* (Publisher: U.S. Department of Commerce, National Oceanic and Atmospheric Administration, National Environmental Satellite, Data and Information Service) doi: 10.7289/V5251G4D